ACS APPLIED MATERIALS & INTERFACES

www.acsami.org

Research Article

Flexible Control of Broadband Polarization in a Spintronic Terahertz Emitter Integrated with Liquid Crystal and Metasurface

Yun Sun, Yong Xu, Helin Li, Yongshan Liu, Fan Zhang, Houyi Cheng, Shina Tao, Huacai Wang, Wei Hu, Yanqing Lu, Chao Zhao, Tianxiao Nie,* Weisheng Zhao,* Qi Guo,* and Lianggong Wen*

Cite This: *ACS Appl. Mater. Interfaces* 2022, 14, 32646−32656

Read Online

ACCESS | Metrics & More | Article Recommendations | Supporting Information

ABSTRACT: Flexible polarization control of the terahertz wave in the wide bandwidth is crucial for numerous applications, such as terahertz communication, material characterization, imaging, and biosensing diagnosis. However, this promise is impeded by the operating bandwidth of circular polarization states, control modes, and the efficiency of the regulation. Here, we report a spintronic terahertz emitter integrated with phase complementary elements, consisting of a liquid crystal and metasurface, to achieve broadband polarization control with high flexibility. This strategy allows the broadband conversion between linear, elliptical, and circular polarization by changing the rotation angle to modulate the space-variant Pancharatnam−Berry phase. The device is characterized with a terahertz time-domain spectroscopy system, demonstrating that the ellipticity of the circular polarization state could keep greater than 0.9 in 0.60−0.99 THz. In the case of an external electro-magnetic field, further polarization modulation experiments are carried out to provide multiple conversion approaches for multi-azimuth. We first propose a method of full broadband polarization state control of the terahertz emitter based on Pancharatnam−Berry phase modulation and an external electro-magnetic field. We believe that such integrated devices with broadband working bandwidth and multiple control modes will make valuable contributions to the development and multi-scene applications of ultrafast terahertz technologies.

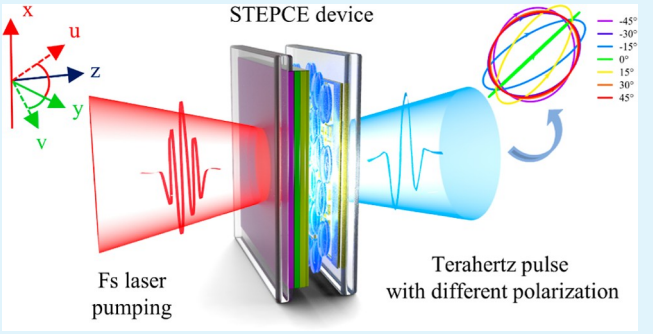

KEYWORDS: *broadband polarization manipulation, spintronic terahertz, liquid crystal, metasurface, terahertz emission, terahertz integrated emitter*

INTRODUCTION

Terahertz science and technology play an important role in regulating light−matter interactions and are the foundation for many sciences and practical applications, such as imaging,[1−3] sensing,[4,5] information multiplexing,[6,7] and communication.[8,9] Terahertz waves can be used to identify a wide variety of material compositions and structures because of their spectral fingerprint and non-invasive properties.[10,11] This field of spectroscopy attracts great interest because the vibrational and rotational modes of chiral molecules and materials are in the terahertz regime, from proteins to amino acids.[12] Furthermore, chiral media behave differently to different circularly polarized (CP) lights, showing remarkable spectroscopic and biological responses.[13] This application is especially relevant for the terahertz spectrum, which exhibits low-energy, non-ionizing, high penetration, and high resolution.[14,15] However, generating broadband CP light with high flexibility in the terahertz regime still suffers from many challenges.

In the last few decades, metasurfaces, composed of artificial subwavelength structures, provide a versatile and efficient approach to control an electro-magnetic wave; therefore, it has been extensively and rapidly developed in the field of photonics.[16−18] Designing structures of metasurface for transmitted and reflected waves could provide design flexibility and realize a variety of fascinating and distinguished applications in terahertz technology, such as metaholograms,[19,20] focusing lenses,[21,22] beam splitters,[23,24] and polarization control.[25−27] However, in the broadband polarization control realized by metasurfaces,[28,29] the metasurfaces act normally as a modulator or polarization converter. They do not realize the generation and active manipulation of the polarized terahertz wave. When active control factors are introduced, such as liquid crystals (LCs),[30−32] graphene,[33] and microelectromechanical systems,[34] the CP terahertz waves often perform in the narrowband. Thus, it is crucial to develop terahertz emission sources that could work actively and with full broadband polarization states.

Received: March 17, 2022
Accepted: June 13, 2022
Published: June 23, 2022

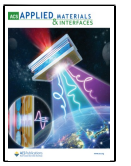

https://doi.org/10.1021/acsami.2c04782
ACS Appl. Mater. Interfaces 2022, 14, 32646−32656

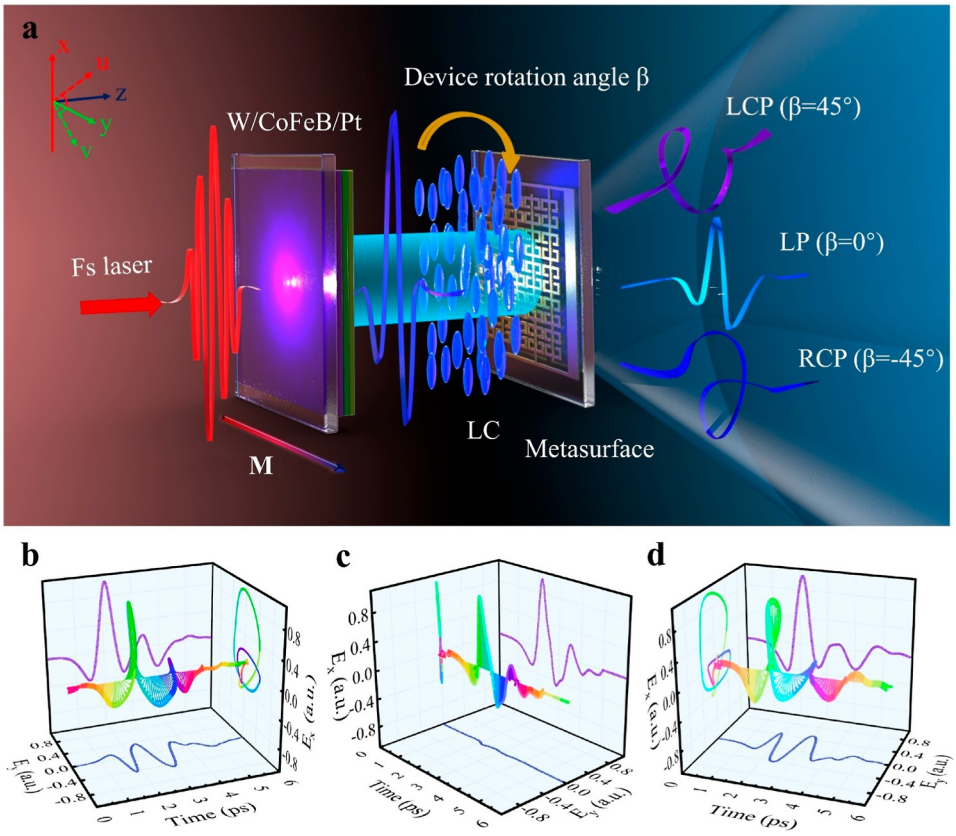

Figure 1. Schematic diagram of polarization manipulation in a STE integrated with LC and metasurface array. (a) Femtosecond laser along the *Z* axis, passes through the spintronic nanofilms and radiates the LP terahertz wave which is perpendicular to the magnetization **M**. As a terahertz wave passes through the LC and the metasurface, phase accumulation occurs due to the birefringence and resonance characteristics of LC and the metasurface. Moreover, the polarization state and chirality of the terahertz wave can be controlled by rotating the device with angle β to modulate the P−B phase of the device. When applying the electro-magnetic field, the LC director will reorient along the field, which can provide highly flexible polarization control. The *u*- and *v*-axes are the directions with angle −45 and 45° based on the y direction, respectively. (b−d) Keeping the direction of the external magnetic field along the *y*-direction, the terahertz time-domain signals with device rotation angles β from 45, 0 to −45° are obtained experimentally, corresponding to (b) LCP, (c) LP, and (d) RCP, respectively.

As well demonstrated, a spintronic terahertz emitter (STE) has the advantages of being easy to integrate[35] and convenient to control.[35−37] It enables additional freedom in polarization flexibility and speed when integrating with LCs.[38] However, the phase retardation obtained by LCs makes the CP terahertz wave dependent on frequency and could work only at the designed frequency point. Very recently, a highly flexible spintronic-metasurface terahertz emitter[39] has been reported and the ellipticity could reach greater than 0.75 from 1 to 5 THz. This approach enabled actively tuning of the terahertz polarization state and helicity by varying the transient currents with an orientated external magnetic field. However, the operation of active tuning is fundamentally limited by changing the external magnetic field arrangement and hard to achieve flexible and fast control of the external field.

In this work, we demonstrate STE integrated with phase complementary elements (STEPCEs), by which both the polarization states and chirality of the terahertz wave can be actively controlled in the broadband frequency-domain. By combining the dynamic phase of LC and the resonance phase of the metasurface, the designed metasurface with birefringence could complement the frequency-dependence of LCs. Based on the phase complementary elements (PCEs) of LC and metasurface, the linear polarization (LP), elliptical polarization (EP), and circular polarization (CP) terahertz wave with left and right-handed can be converted by space-variant Pancharatnam−Berry (P−B) phase modulation in 0.60−0.99 THz. The performance of the polarization control is characterized by the ellipticity and Poincaré sphere. The results show that the absolute value of the ellipticity for the left-handed CP (LCP) and right-handed CP (RCP) can be kept greater than 0.9 over the working bandwidth. Further experiments of electro-magnetically controllable polarization are conducted to verify the possibility of the multiple control modes with high flexibility. What is more, the results are reflected by the Poincaré sphere, which shows that multi-azimuth control can be achieved from near two poles to the equator. The device architecture presented in this paper has the potential to be used as carrier for material characterization and identification. This device, capable of generating a CP wave with different chiralities in a wideband, can also be used to test the circular dichroism of biological samples, which has important applications for continuously tunable biosensing. Moreover, the device provides multi-mode control, which provides higher applicability for different applications in multiple scenarios. In comparison, the electrical control provides a faster modulation rate which plays an important role in the development and application of optoelectronic devices.

https://doi.org/10.1021/acsami.2c04782
ACS Appl. Mater. Interfaces 2022, 14, 32646−32656

MATERIALS AND METHODS

The configuration of the polarization manipulation STE integrated with LCs and metasurface is illustrated in Figure 1a. The STEPCE device consists of two glass substrates separated by a 250 μm thick spacer and infiltrated with the high-birefringence LCs. When a femtosecond laser is incident on the STE, the spin-polarized current $\vec{j}_s$ injected in the ferromagnetic layer is transformed into the transverse charge current $\vec{j}_c$ in the nonferromagnetic (NM) layer due to the inverse spin-Hall effect.[40] The conversion relationship between the two currents is $\vec{j}_c = \gamma \vec{j}_s \times \vec{M}/|\vec{M}|$, where $\vec{j}_c$ is the converted charge current, $\vec{\gamma}$ is the spin Hall angle of NMs, $\vec{j}_s$ is the longitudinal spin-polarized current, and $\vec{M}$ denotes the sample magnetization. The emission mechanism of the STE is detailed in Supporting Information, S1. Then, the linear terahertz wave passes through LCs and metasurface to accumulate phase delay in two perpendicular directions due to the birefringence and resonance characteristics. In order to control the accumulated phase, we introduce a geometric phase in the space domain related to the polarization of light, which is the space-variant P−B phase.[25] The space-variant P−B phase is not introduced through optical path differences or resonance responses but results from the geometric phase that accompanies space-variant polarization manipulation.[41] Based on the derivation and verification of the metasurface phase compensation and space-variant P−B phase, the tuning of the phase delay could be realized by angle rotation, thus radiating terahertz waves with different polarization states and chiralities. Due to the sensitivity of LC to applied electro-magnetic field, the phase delay can also be changed by applying voltage or magnetic field to change the arrangement of LCs.[42]

The principle applied here is that two conditions need to be satisfied to control the broadband polarization states and chirality. One is the emission of the linearly polarized terahertz wave and the other is the broadband phase retardation which can be manipulated flexibly. In order to achieve terahertz emission and device integration, we choose the STE,[43] with a tri-layer heterostructure of W (2 nm)/CoFeB (2 nm)/Pt (2 nm) nanofilms prepared in a DC and RF sputtering system (TEC-SPU-800) manufactured by Truth Equipment Co.[44] Besides, the LC NJU-LDn-4 with a high mean birefringence of 0.306 in the terahertz region from 0.4 to 1.6 THz, is used to achieve large phase accumulation.[45] Because the dynamic phase delay caused by LC is linearly dependent on the frequency,[46] the metasurface array could be designed to compensate the phase delay of LC and maintain the broadband phase delay.[25] During the transmission of terahertz waves, the action of LC and metasurface on the polarization can be regarded as two cascaded optical systems. Thus, the LCs and metasurface, as the PCEs, provide P−B phase accumulation and change to realize full-state emission and regulation of broadband polarization.

In the initial state, the extraordinary and ordinary transmission axes of the PCE coincide with x- and y-axes, respectively. When the linearly polarized terahertz wave is incident to the LCs, the wave can be decomposed into two parts: parallel and perpendicular to the LC director. When the terahertz wave passes through LCs with the thickness of d, the ordinary and extraordinary components will produce dynamic phase retardation $\Delta\varphi_{LC}$ due to the birefringence of LCs, which can be expressed as $\Delta\varphi_{LC} = 2\pi(n_e - n_o)d/\lambda$, where n_e is the extraordinary refractive index, n_o is the ordinary refractive index, d is the thickness of LCs, and λ is the incident wavelength in vacuum. What is more, the nematic LC molecules will rotate and reorient along the direction of the applied electro-magnetic field when the voltage or magnet is applied.[42,47] As a result, the LC molecules will deflect at an angle θ which is related to the direction and magnitude of the applied field, and the dynamic phase retardation $\Delta\varphi_{LC}$ will change accordingly.[48] Therefore, the transfer Jones matrix of LC can be represented as[49,50]

$$\boldsymbol{T}_{LC} = \begin{pmatrix} e^{i2\pi n_e'(\theta)d/\lambda} & 0 \\ 0 & e^{i2\pi n_o'(\theta)d/\lambda} \end{pmatrix} \quad (1)$$

where $n_e'(\theta)$ and $n_o'(\theta)$ represent the switched extraordinary and ordinary refractive index related to the deflection angle θ along x- and y-axes, respectively. As for the metasurface, the anisotropic configuration and different resonance modes would lead to the birefringence between two vertical linear eigen polarizations in the x- and y-axes.[25,51] The unit cell was optimized to achieve the equal transmission amplitudes along x- and y-directions and realize complementary resonance phase difference with LCs. When designing and simulating the meta-atom, the diagonal transmission coefficients are ignored because of the weak cross-polarization coupling. Thus, the transmittance of basic meta-atom can be described as[26,34]

$$\boldsymbol{T}_{meta} = \begin{pmatrix} |t_{xx}|\, e^{i\varphi_{xx}} & 0 \\ 0 & |t_{yy}|\, e^{i\varphi_{yy}} \end{pmatrix} \quad (2)$$

where t_{xx}, t_{yy}, φ_{xx}, and φ_{yy} denote the linear transmission amplitudes and phase retardations of metasurface for the eigen-polarized waves along the x- and y-directions, respectively. Besides, the transmission characteristic of PCE can be described by the Jones matrix $\boldsymbol{T}_{PCE}$, as follows[52]

$$\begin{pmatrix} E_x^{out} \\ E_y^{out} \end{pmatrix} = \boldsymbol{T}_{PCE} \begin{pmatrix} E_x^{in} \\ E_y^{in} \end{pmatrix} \quad (3)$$

where E_x^{in}, E_y^{in}, E_x^{out}, and E_y^{out} are the x- and y-polarized components of the incident and transmitted terahertz waves, respectively. Moreover, the Jones matrix $\boldsymbol{T}_{PCE}$ is related to the transmission responses of the LCs and metasurface. Therefore, it can be obtained based on the above equations and the rotation matrix $\boldsymbol{R}_\beta = \begin{pmatrix} \cos\beta & -\sin\beta \\ \sin\beta & \cos\beta \end{pmatrix}$, which can be described as[53]

$$\boldsymbol{T}_{PCE} = \boldsymbol{R}_\beta \boldsymbol{T}_{meta} \boldsymbol{T}_{LC} \boldsymbol{R}_{-\beta} \quad (4)$$

where β is the rotation angle between the extraordinary axis of PCE and the x-axis. In the process of spatial change through angular rotation, the transmission properties and phase of PCE will be changed, which is consistent with the proposed space-variant P−B phase modulation. Thus, the LCs and designed metasurface could provide phase complementary and realize space-variant P−B phase modulation with angle rotation. In a word, the conversion between LP, EP, and CP of the terahertz waves can be achieved. As shown in Figure 1b−d, we experimentally obtained the terahertz time-domain signal with β from 45, 0 to −45° based on the y-axis, corresponding to LCP, LP, and RCP. The phase difference between the signals in the projection of yz plane and the xz plane can be observed clearly. Moreover, in the Lissajous projection images of the xy plane, we can see that three kinds of signals have different polarizations and rotation directions. Besides, when the deflection angle θ of LC is changed by adjusting external field conditions, the existing polarization states can be controlled with high flexibility. The following sections will show how we achieve the full-state emission and multiple modes regulation of broadband polarization through detailed experimental investigations.

RESULTS AND DISCUSSION

Characterization of Phase Complementary Meta-Atom. The phase complementary motivated us to design our meta-atom based on the split ring resonator (SRR) metasurface.[54−56] The SRR would exhibit different resonance modes based on the eigen polarization of the incident wave. We designed our meta-atom with birefringence based on the work in the microwave region and optimized the structure as we expected.[51,57] The meta-atom introduces inductor−

https://doi.org/10.1021/acsami.2c04782
ACS Appl. Mater. Interfaces 2022, 14, 32646−32656

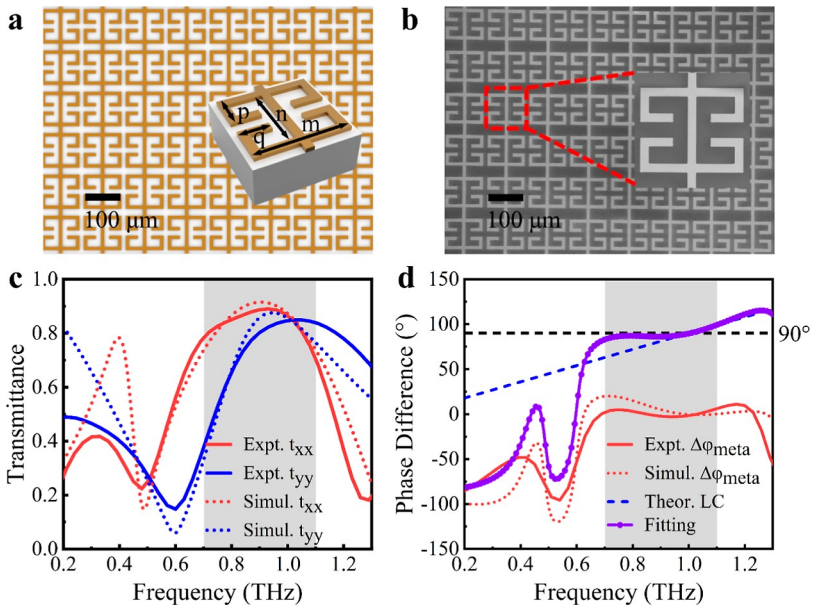

Figure 2. Meta-atom design and its optical properties. (a) Schematics of the designed phase complementary meta-atom and array (m = 108 μm, n = 68 μm, p = 26.5 μm, and q = 35 μm), and the cell period is 120 μm, the linewidth is 10 μm. (b) SEM images of part of the fabricated metasurface consisting of a periodic array of the designed meta-atoms and the illustration displaying the SEM of a unit cell. (c) The measured and simulated transmission amplitude spectra of x- and y-polarized terahertz waves are expressed by solid lines and dotted lines, respectively. (d) Experimental (solid lines) and simulated (dotted line) phase difference of metasurface, of which $\Delta\varphi = \varphi_{yy} - \varphi_{xx}$. Also, the fitting phase is obtained by combining the simulated phase difference of the metasurface with the theoretical P−B phase of the LCs.

capacitor (L−C) resonance and dipole resonance with the eigen polarization of the incident terahertz wave along the x- and y-axis, respectively.[28,58] In consequence, the polarization-dependent resonances will produce the birefringence property to achieve the phase complementary with LCs. At the same time, we should avoid the working frequency band at resonance due to the high efficiency of transmission. After investigation and optimization, the rectangular design was chosen to achieve flexible phase difference control and ensure high transmission efficiency.[28] With careful structural tuning, the ultimate design for the meta-atom was obtained and the unit cell was connected and configured as the electrodes of the LCs. Figure 2a depicts part of our array and the inset is the schematic diagram of the unit structure. After that, we fabricated an array containing 75*75 periodic unit cells (periodicity of 120 μm) of the designed meta-atoms by standard photolithography on a quartz glass. The scanning electronic microscopy (SEM) (Zeiss Sigma 300, Germany) photographs of the metasurface are shown in Figure 2b.

We also performed a numerical simulation with the finite element method (FEM). In the model, a unit cell with realistic structures on the quartz glass was included, and periodic boundary conditions were employed for the simulation of the connected metasurface array. The material parameters used in the simulation were metal by the Drude model, quartz glass substrate as a lossy dielectric material with a permittivity of 4.46, and the loss tangent is ≈0.0004.[34,59−61] Then, the transmittance of the two orthogonal eigen-polarization is simulated by frequency solver. We combined the simulation with the theoretical phase retardation of LC in eq 1 with d = 250 μm, n_o = 1.56, n_e = 1.88 to keep 90° at 1 THz. The dimensions of the meta-atom were optimized for the designed working frequency. We changed the SRR area, period and the effective length of the structure to optimize the L−C resonance and the dipole resonance, respectively. Figure 2c,d shows simulation results of the optimized transmittance amplitudes and phase difference for x- and y-polarizations with dotted lines. The cross-polarization coefficients are negligibly small owing to the symmetric nature of the metasurface around both x- and y-axes.

We then use a terahertz time-domain spectroscopy (THz-TDS) system (Figure S1a) to characterize the transmission properties of our fabricated metasurface array with different eigen polarizations. The study of the terahertz emission and modulation of the device were carried out with a home-built THz time-domain spectrometer.[62] The femtosecond laser pulse used in the experiment is generated by an amplified Ti:sapphire laser source with 800 nm central wavelength, a 35 fs pulse duration, and an 1 kHz repetition rate. We pumped the W (2 nm)/CoFeB (2 nm)/Pt (2 nm) STE with a 170 mW, 8 mm diameter laser and a static in-plane field of 100 mT magnetization (NdFeB magnet). Moreover, the terahertz pulse was detected with a 2 mm ZnTe crystal through electro-optic sampling. The measured time-domain signal emitted by the STE and the Fourier transform spectrum can be found in Figure S1c,d. All the measurements were carried out in N_2 to avoid water vapor affecting the terahertz signal. Terahertz pulses were focused on the effective area of metasurface, and transmitted pulses were sampled by ZnTe crystal to measure the time-resolved transmission signal. We transformed the measured time-domain signal into the frequency spectrum. The spectrum without passing through the sample, denoted by $\boldsymbol{E}_{ref}(w)$, was measured as the reference. Moreover, the transmitted pulses of metasurface transformed to frequency-domain could be represented by $\boldsymbol{E}(w)$. Therefore, the transmittance of metasurface can be calculated by $\boldsymbol{t}(w) = \boldsymbol{E}(w)/\boldsymbol{E}_{ref}(w)$. For the anisotropy of the designed meta-atom, we measured the transmission properties of the metasurface and it can be expressed as $\boldsymbol{E}_{L-C}(w)$ and $\boldsymbol{E}_{dipole}(w)$ according to the resonance modes in two orthogonal directions. The

https://doi.org/10.1021/acsami.2c04782
ACS Appl. Mater. Interfaces 2022, 14, 32646−32656

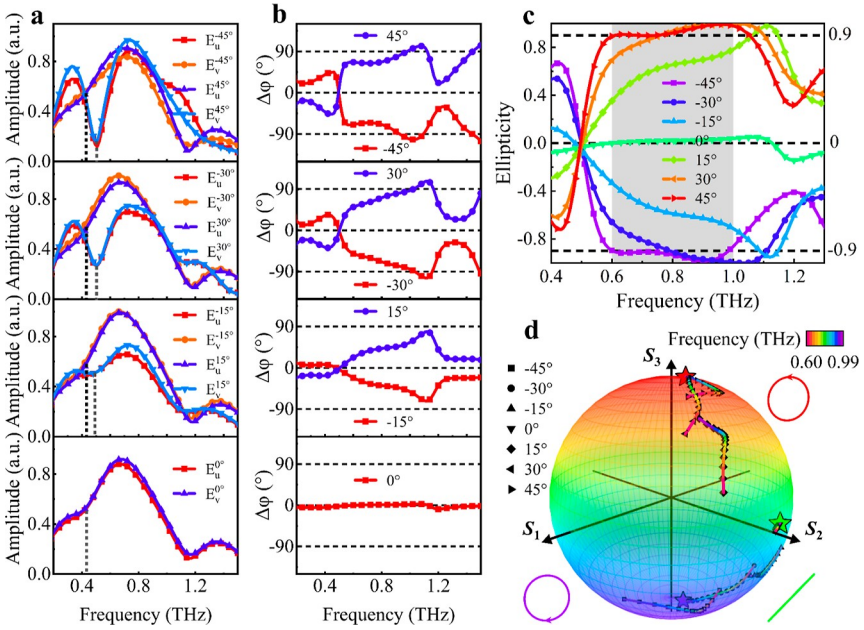

Figure 3. Performance of the broadband phase engineered PCE. (a) Fourier transformed spectra of the amplitudes with β from ±45, ±30, and ±15 to 0° in u- and v-directions. (b) The corresponding phase differences at different angles, $\Delta\varphi = \varphi_v - \varphi_u$, where φ_v and φ_u are the phases transformed in the u- and v-directions, respectively. (c) Seven terahertz waves with different ellipticities at different rotation angles. (d) Poincaré sphere interpretation of the PCE in 0.6−0.99 THz at different rotation angles. Stokes parameters S_1, S_2, and S_3 are the axes of coordinate of the Poincare sphere. The red, green, and purple stars represent the polarization states close to LCP, LP, and RCP, and their corresponding ellipses depicted as red, green, and purple curves, respectively.

transmission coefficients of Jones matrix in eq 3 can be expressed by transmittance

$$\boldsymbol{t}_{L-C}(w) = \boldsymbol{E}_{L-C}(w)/\boldsymbol{E}_{\text{ref}}(w) = |t_{xx}|\, e^{i\varphi_{xx}}$$
$$\boldsymbol{t}_{\text{dipole}}(w) = \boldsymbol{E}_{\text{dipole}}(w)/\boldsymbol{E}_{\text{ref}}(w) = |t_{yy}|\, e^{i\varphi_{yy}} \quad (5)$$

The measured spectra of the transmittance amplitudes t_{xx} and t_{yy} and the phase difference between φ_{xx} and φ_{yy} of the metasurface are shown in Figure 2c,d with solid lines for two orthogonal incident polarizations, respectively. To verify the metasurface anisotropy, the transmission for x- and y-polarized terahertz pulses were measured by rotating the metasurface 90° about the incident terahertz wave. The transmission results for both polarizations are in accordance with the simulation given previously. The resonance frequencies of $L-C$ resonance and dipole resonance are approximately at 0.48 and 0.60 THz, respectively. Obviously, the designed meta-atom exhibits approximately equal transmittance amplitudes but with a complementary phase retardation with LC's theoretical phase at a broadband frequency interval. As can be seen in the figure, the phase responses for LC and metasurface vary in a complementary manner and can be kept close to 90°, and the transmittance amplitudes in the designed band can be roughly consistent, which provides the simulation and theoretical basis for the subsequent emission of broadband CP terahertz waves.

Broadband Manipulation of Polarization States and Chirality. Utilizing the designed metasurface and LCs as a phase complementary component, the integrated device STEPCE was achieved to control the polarization states and chirality of the terahertz wave in wide bandwidth. As for the preparation process of the device, the tri-layer nanofilms were grown on one glass substrate by magnetron sputtering and the other glass substrate was covered with metasurface array through micro−nano fabrication technologies. Both substrates were spin-coated with sulfonic azo dye (SD1) as an alignment layer. Moreover, they were bonded with a 250 μm gap left and photo-aligned in the x-direction to achieve homogeneous pre-alignment. Finally, the LCs were irrigated into the gap between the upper and lower substrates and the device was sealed. See Figure S2 for the specific preparation process of the integrated device. Besides, the effect of the applied magnetic field on the spintronic nanofilms is magnetizing the sample and the magnetic strength has reached saturation when it is less than 10 mT. Therefore, the magnetic strength makes no difference to the intensity of the radiation terahertz wave when it is greater than 10 mT. As for the birefringence of LCs, the external magnetic field has a certain effect on the orientation of the LC director.[63] Thus, we conducted experiments of the effect on the magnetic strength on the LCs and finally determined to keep the external magnetic field at 20 mT to avoid the re-orientation of the LCs. See Supporting Information, S3 for relevant experiment results.

The polarization characteristics of the integrated devices are still measured by the THz-TDS system. Different from the transmittance measurements of metasurface, 2 THz polarizers combined a polarization-resolved system is used to detect the terahertz polarization states: one can be adjusted between −45° (u axis) and 45° (v axis) based on the y-direction, while the other is fixed to detect the perpendicularly polarized terahertz waves. Because the LCs between the spintronic nanofilms and the metasurface can be regarded as a Fabry−Perot-like microcavity, the reflection peak was eliminated during testing and data processing. Figure 3a,b illustrates the terahertz spectra and their corresponding phase differences of the seven polarization states with the rotation angle β changing from ±45, ±30, and ±15 to 0°. The amplitudes E_u and E_v are obtained from the Fourier transform of the time-domain

https://doi.org/10.1021/acsami.2c04782
ACS Appl. Mater. Interfaces 2022, 14, 32646−32656

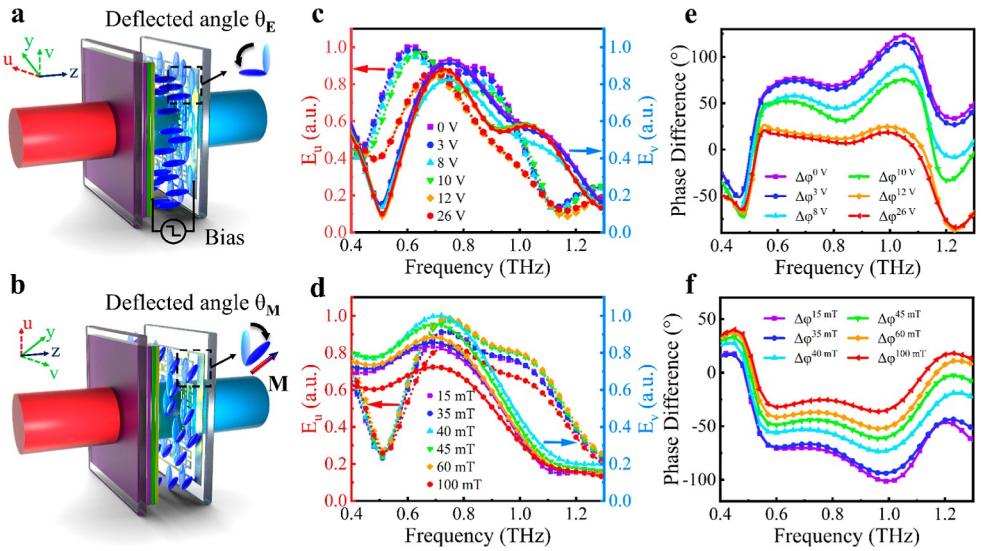

Figure 4. Schematic diagram and performances of the applied electro-magnetic field. (a,b) Schematic diagram of the applied electric field and the magnetic field. (c,d) The Fourier transformed spectra of the amplitudes measured in the *u*- (dotted lines) and *v*- (solid lines) directions at different voltages and different magnetic strengths. (e,f) The phase difference between the Fourier transform of the signal in the *v*- and *u*-direction.

signals measured in *u*- and *v*-directions, and the phase difference is extracted as $\Delta\varphi = \varphi_v - \varphi_u$, where φ_v and φ_u are the phases corresponding to the Fourier transformed phases. In that bandwidth, the amplitudes and phase differences of the two vertical directions change correspondingly with the rotation angle, which is related to the content of different resonance modes and refractive indexes. All the data are normalized with respect to a reference.

When β is −45°, the components of the incident wave decomposition in the ordinary and extraordinary optical axis of the device are approximately equal; thus, the signals measured in the *u*- and *v*-axes will reflect the resonance characteristics of the metasurface and the birefringence properties of LCs. The amplitude of the Fourier transformed spectrum measured on the *u*-axis shows the dipole resonance at 0.51 THz; meanwhile, the amplitude on the *v*-axis indicates the *L*−*C* resonance at 0.43 THz. The remaining peak positions are related to the properties of the electro-optic sample crystal. The position of the resonance peak measured by the integrated STEPCE is red-shifted compared with that measured by the metasurface. That is because the metasurface of the integrated device is infiltrated in the LCs, which will provide a higher refractive index than the air in the polarization direction of the terahertz wave, resulting in a corresponding frequency shift.[64] As β changing from −45 to 0°, the signal measured in *u*- and *v*-directions will contain both resonance components but the amount varies with the angle. Until β is 0, the dipole and *L*−*C* resonance components measured in the *u*- and *v*-axes are the same. Due to the anisotropy of the device, as β changing from 0 to 45°, the signal measured on the *u*- and *v*-axes is roughly consistent with the corresponding negative angle *v*- and *u*-axis signals, verifying the success of the device preparation.

Considering that the non-resonant frequency has less sensitive shift and higher transmission efficiency, the working frequency range for realizing broadband polarization control is the non-resonant frequency band of 0.60−0.99 THz. To assess the performance of the broadband polarization control, we calculated the Stokes parameters[65] from the above experiment of P−B phase modulation. The Fourier transformed spectra E_u and E_v and their corresponding phases φ_v and φ_u can be used to describe the two orthogonal components of the terahertz wave, as $\boldsymbol{E} = E_u\, e^{i\varphi_u} + E_v\, e^{i\varphi_v}$. Therefore, the Stokes parameters can be calculated by the following equations

$$S_0 = E_u^2 + E_v^2,\ S_1 = E_u^2 - E_v^2$$
$$S_2 = 2E_uE_v\ \cos\Delta\varphi,\ S_3 = 2E_uE_v\ \sin\Delta\varphi \quad (6)$$

Moreover, the ellipticity is defined as $\chi = S_3/S_0$. The ellipticity is positive for the left-handed polarized waves, while negative for the right-handed, specially, $\chi = 1$ denotes that the emission terahertz wave is an ideal LCP, $\chi = 0$ for LP, and $\chi = -1$ for an ideal RCP. As shown in Figure 3c, the ellipticity keeps lower than −0.9 at −45°, almost equal to 0 at 0° and higher than 0.9 at 45° from 0.60 to 0.99 THz, which means that the conversion between CP, EP, and LP with different chiralities could be achieved in this broadband. What is more, Poincaré sphere is the most intuitive way to cover all the polarization states and to represent the modulation trajectories of the polarization states.[41,66] The broadband manipulation is interpreted in the Poincaré sphere as shown in Figure 3d, where a complex Jones vectors is mapped to the surface of the sphere using Stokes parameters S_1, S_2, and S_3 as three axes of Cartesian coordinates. The transformation trajectory is mapped on the surface of the Poincaré sphere with different rotation angles β between 0.60 and 0.99 THz. When β is ±45°, the trajectories located near the north and south poles of the sphere, and when β approaches to 0°, the trajectory is toward the equatorial direction. Three points approximate to LCP, LP, and RCP are marked out and the ellipticities are characterized by curves of corresponding colors. Due to the symmetry of the device, the red and purple stars indicate the approximate ellipticity of 0.99 and −0.99 at 0.99 THz with rotation angle ±30°, respectively. Moreover, the green star represents the ellipticity of 0 at 0.60 THz with no rotation angle. In addition, the polarization states of the three stars are represented by curves of the corresponding colors in the illustration, proving that the device can be demonstrated to convert from CP, EP, and LP with different chiralities. According to the design principle for broadband controlling the polarization states and chirality, we first successfully demonstrate the broadband

https://doi.org/10.1021/acsami.2c04782
ACS Appl. Mater. Interfaces 2022, 14, 32646−32656

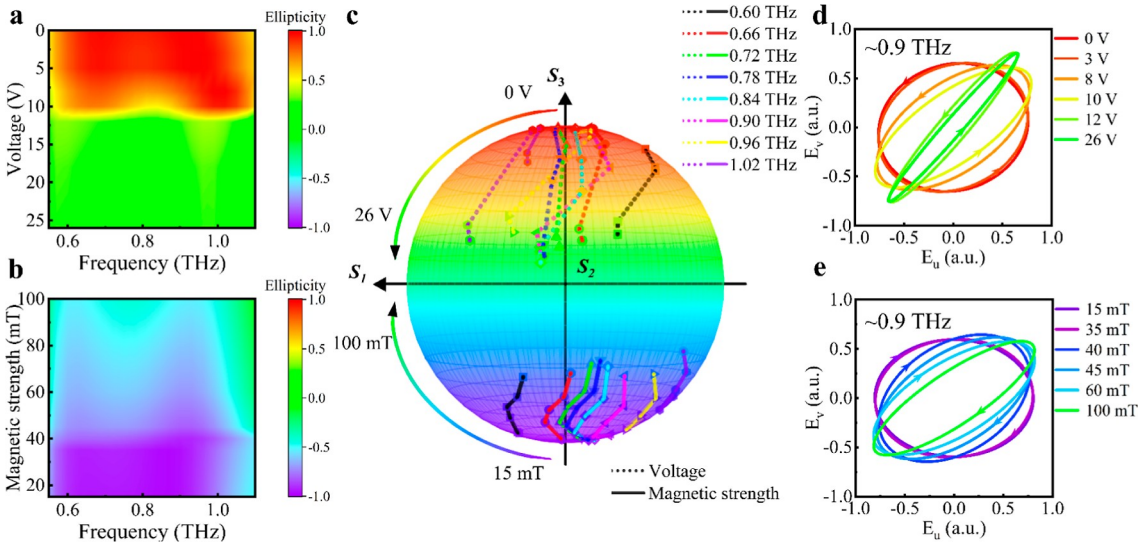

Figure 5. Performance of highly flexible broadband manipulation by an external electro-magnetic field. (a,b) The ellipticities change with different voltages and magnetic strengths at 0.5−1.2 THz. (c) The effects of voltage and magnetic strength on the ellipticities were characterized from 0.6 to 1.02 THz with 0.06 THz interval. (d,e) The electric field of the transmitted wave for different voltages. Polarization states at 0.9 THz for different incident voltages and magnetic strengths, demonstrating the capability of tuning the polarization states and chirality.

modulation of polarization and chirality through space-variant P−B phase modulation with angle rotation.

Highly Flexible Polarization Control with Multiple Modes. The tunability of the polarization states and chirality exists not only for the P−B phase modulation of the device but also for the applied electro-magnetic field modulation of LCs. The above schematic diagrams with multiple control modes of LC directors driven by electric field and magnetic field are shown in Figure 4a,b, respectively. Because of the integrated characteristics of the device and the electrical conductivity of the metal, the STE and metasurface can also be used as electrodes to apply the external bias. The initial arrangement of the LC directors is consistent with the extraordinary axis of the device. The additional square wave voltage with 1 kHz period was applied through a signal generator and a high voltage amplifier. Moreover, the magnetic strength was adjusted by changing the number of static magnets. According to the P−B phase manipulation, when the rotation angle between the extraordinary axis and the x-axis is 45° (v axis) and −45° (u axis), the radiation terahertz wave could almost approach to LCP and RCP. Based on the above experiments, we realized the modulation between CP, EP, and LP with high flexibility by an external electro-magnetic field when the direction of LC is along v- and u-axes, respectively.

Keeping the polarization direction of incident wave along x-axis, the amplitudes and phase differences manipulation of the electric field in z-direction and magnetic field in y-direction are shown in Figure 4c−f, respectively. In the process of electric field modulation, the refractive index in E_v direction changed from extraordinary one n_e to ordinary one n_o, so there is a trend of shift in amplitude at the resonance peak. While the refractive index in z direction changed from n_o to n_e, the resonance curves keep a tendency to blue shift. In the polarization modulation of 0.60−0.99 THz because the LCs changed gradually toward the z-axis of transmission direction, the amplitude variations of E_u and E_v are consistent with the voltage variation, and the phase difference decreases gradually. Moreover, during the modulation of the magnetic field, the amplitudes of the two vertical directions in the working frequency band remain roughly the same, and the phase differences decrease gradually with the increase of the magnetic strength.

On the basis of P−B phase broadband modulation, examples of tunable polarization with high flexibility are presented in Figure 5a,b, showing the tunable polarization states of transmitted waves for different electro-magnetic fields. For example, at 0.55−1.10 THz, the emitted wave is close to LCP for the rotation angle of 45° when the applied voltage is 0 V. An increase in the voltage (from 0 to 26 V) gradually tunes the polarization states to the left-handed EP. When the applied voltage is 26 V, the ellipticity of the terahertz wave is close to 0 which means that the wave is nearly LP. Moreover, it is similar for the manipulation of the magnetic field, which roughly reveals the polarization control from the RCP to the right-handed EP to the LP at −45° as the magnetic strength increases. In Figure 5c, we further reflect the effect of an external electro-magnetic field on the polarization states in the Poincaré sphere between 0.60 and 1.02 THz with 0.06 THz intervals. As can be seen from the Poincaré sphere, with the increase of applied voltage or magnetic strength, the trajectories gradually change from the two poles to the equator, indicating that multi-azimuth control can be achieved. With the increase of the excitation of external electro-magnetic field, the ellipticity of each frequency point decreases and the dynamic phase accumulation of LC is decreasing. As schematic illustrated in Figure 5d,e, we characterize the curve of ellipticities at 0.9 THz as it varies with voltage and magnetic strength. In short, the results in Figure 5 reflect the polarization states regulation effect obtained by an external electro-magnetic field at a single frequency point. Therefore, the polarization states can also be controlled by applying an external electro-magnetic field to modulate the dynamic phase delay of LC. Moreover, changing the applied electro-magnetic field is faster and easier than rotating a magnet or device. It supplements and enriches the broadband polarization control and chirality tunability of the integrated device STEPCE, which enables creating a polarization and chirality manipu-

https://doi.org/10.1021/acsami.2c04782
ACS Appl. Mater. Interfaces 2022, 14, 32646−32656

lation terahertz emitter with a wideband and high flexibility as we now discuss.

CONCLUSIONS

In this paper, we proposed a polarization-regulated terahertz emitter consisting of STE, LC, and metasurface and demonstrated that this integrated device STEPCE could achieve multi-polarization states and chiral manipulation with high flexibility over a wideband. The meta-atom was designed with an anisotropic response by simulation and its resonance phase was theoretically fitted with the theoretical dynamic phase properties of LCs to achieve the expected phase complementation. Although the metasurface has flexibility to design, the change of the medium will also affect the location of its resonance, which should be noticed in future work. Based on the above design and fabrication of the integrated device STEPCE, we have experimentally proved that the conversion between linear, elliptical, and CP could be realized in 0.60−0.99 THz by space-variant P−B phase modulation with angle rotation. When the angle β is ±45°, the absolute value of the ellipticity could reach greater than 0.9 with different chiralities, and when the β is 0°, the ellipticity almost remains 0. Because LCs is sensitive to external electro-magnetic field, we further proposed multiple modes control for broadband polarization states by voltage and magnetic strength under different rotation angles. The results of polarization control are characterized by Poincaré sphere, proving that multi-azimuth control can be achieved from near two poles to the equator. In addition to flexible control of the broadband spintronic terahertz polarization states, the proposed phase complementary, design flexibility of metasurface, easy integration elements, and multiple modes control offer the potential for the development of diversified terahertz functional devices, facilitating the development and applications of spintronics and terahertz technologies.

EXPERIMENTAL SECTION

Device Fabrication. The fabrication process of the integrated device STEPCE is schematically illustrated in Figure S2 in the Supporting Information. The fabrication of the device comprised three parts: the sample growth of STE, the manufacture of the metasurface, and the infiltration of LC. First, the glass substrates (500 μm thick) were cleaned using acetone and isopropyl alcohol in advance to remove contamination. The W (2 nm)/CoFeB (2 nm)/Pt (2 nm) nanofilms were deposited at room temperature in a DC and RF sputtering system (TEC-SPU-800) manufactured by Truth Equipment Co., LTD with an ultimate vacuum of 1×10^{-10} mbar and without any magnetic fields. The deposition rates were 1.4 nm/min for W at an Ar pressure of 2 mbar, 0.7 nm/min for $Co_{20}Fe_{60}B_{20}$ at an Ar pressure of 2 mbar, and 3.8 nm/min for Pt at an Ar pressure of 2 mbar. An alloy target with the composition of $Co_{20}Fe_{60}B_{20}$ (in atomic percent) was used to deposit the $Co_{20}Fe_{60}B_{20}$ layer.

Furthermore, the standard photolithography technique was used to fabricate the metasurface. A lithographic sacrifice layer (LOR5B, MicroChem) and a layer of positive photoresist (AZ5214E, Clariant GmbH) were spun onto the cleaned substrate, respectively. The bilayer configuration facilitates the subsequent lift-off process. The designed patterns were transferred to the substrate with the ultraviolet (UV) exposure time of 15 s. After developing, the electron beam evaporation process was applied to deposit 20/200 nm of Cr/Au, and lift-off. The total metasurface area was 7.2 mm × 7.2 mm, containing 60 × 60 individual unit cells. Besides, the wires in the middle of the metasurface unit were connected to each other and lead out at both ends as electrodes.

After that, the spintronic nanofilms and metasurface are spin-coated at 3000 rpm for 30 s with SD1 (Dai-Nippon Ink and Chemicals, Japan) to orient the LC director and baked at 100 °C for 10 min to remove the solvent. Then, the cell was assembled by two processed substrates with a 250 μm thick Mylar spacer. After that, a UV exposure was applied to introduce homogeneous alignment which was parallel to the x-direction. The LC NJU-LDN-4 with large birefringence was infiltrated at 180 °C, and the device was sealed after cooling to room temperature. As a result, the integrated device was obtained.

Numerical Simulation. A numerical simulation was performed with the FEM in order to gain the resonance phenomenon and inform optimal device parameters. A base unit cell was defined with Floquet boundary conditions used to simulate an infinite metasurface array. The numerical simulations were performed by a time-domain solver with periodic boundary conditions for each unit cell. The dimensions of each meta-atom are specified in the main text and material properties are the same as the experimental samples. Besides, the permittivity of quartz glass was set to 4.46. The Drude model was employed to represent the complex conductivity of gold. The incoming THz radiation was simulated with a top port emitting E_x and E_y polarized plane waves toward the meta-atom. The corresponding x- and y-axis transmission signals were extracted to calculate the phase retardation and theoretical fitting with LCs.

TERAHERTZ MEASUREMENT

A home-built THz time-domain spectrometer based on STE was used to measure the transmission properties of our fabricated devices. The optical path and emission performance of the system can be seen in Supporting Information, S1. An ultrafast 35 fs laser pulse generated by a typical Ti:sapphire laser amplifier system with central wavelength of 800 nm and repetition ratio of 1 kHz (6 W average power) was divided into a pump beam (90%) to excite the spintronic terahertz signal and a probe beam (10%) to measure the time-domain signal. The STE was magnetized by a static NdFeB magnet, and the subsequent experiments of changing magnetic strength were also realized by changing the number of the magnets. Moreover, the STE was illuminated by the linearly polarized pump beam to radiate terahertz waves along the propagation of the z-axis. The polarization-resolved system combined with two polarizers was employed to divide the generated terahertz electric field into two orthogonal components of E_u and E_v in the u- and v-directions, in which the first polarizer was adjusted between −45 and 45°, and the second one was fixed in the x-direction which was consistent with the direction of emission. While the terahertz wave and the probe beam were collinear through the 2 mm ZnTe detector for electro-optic sampling, which includes a quarter-wave plate, a Wollaston prism, and a balanced detector. The extinction ratio of the polarizers was ≈1000. Therefore, the obtained terahertz electric fields parallel or perpendicular to the magnetic fields are $E_x = E_u - E_v$ and $E_y = E_u + E_v$, respectively.[36] In the experiment of applying voltage to control LCs, a square wave voltage with 1 kHz period was applied with a signal generator (UTG7025B, UNI-T) and a high voltage amplifier (ATA2041, Aigtek). The experiments were carried out at room temperature; meanwhile, the airtight chamber where the optical path was placed was filled with N_2 to eliminate the effect of water vapor.

ASSOCIATED CONTENT

Supporting Information

The Supporting Information is available free of charge at https://pubs.acs.org/doi/10.1021/acsami.2c04782.

https://doi.org/10.1021/acsami.2c04782
ACS Appl. Mater. Interfaces 2022, 14, 32646−32656

Schematic diagram of the polarization-resolved THz-TDS system, corresponding time and frequency domain signals of the STE, fabrication process of the STEPCE device, experimental schematic diagram of magnetic field on LC, and the corresponding phase changes (PDF)

AUTHOR INFORMATION

Corresponding Authors

Tianxiao Nie − *School of Integrated Circuit Science and Engineering, Beihang University, Beijing 100191, China; Beihang Hangzhou Innovation Institute Yuhang, Beihang University, Hangzhou 310023, China; Hefei Innovation Research Institute, Beihang University, Hefei 230013, China;* orcid.org/0000-0001-9067-9931; Email: nietianxiao@buaa.edu.cn

Weisheng Zhao − *School of Integrated Circuit Science and Engineering, Beihang University, Beijing 100191, China; Beihang Hangzhou Innovation Institute Yuhang, Beihang University, Hangzhou 310023, China; Hefei Innovation Research Institute, Beihang University, Hefei 230013, China;* orcid.org/0000-0001-8088-0404; Email: weisheng.zhao@buaa.edu.cn

Qi Guo − *School of Instrumentation and Optoelectronic Engineering, Beihang University, Beijing 100191, China*; Email: qguo@buaa.edu.cn

Lianggong Wen − *School of Integrated Circuit Science and Engineering, Beihang University, Beijing 100191, China; Beihang Hangzhou Innovation Institute Yuhang, Beihang University, Hangzhou 310023, China;* orcid.org/0000-0002-5669-7340; Email: wenlg@buaa.edu.cn

Authors

Yun Sun − *School of Integrated Circuit Science and Engineering, Beihang University, Beijing 100191, China; Beihang Hangzhou Innovation Institute Yuhang, Beihang University, Hangzhou 310023, China; Hefei Innovation Research Institute, Beihang University, Hefei 230013, China*

Yong Xu − *School of Integrated Circuit Science and Engineering, Beihang University, Beijing 100191, China; Hefei Innovation Research Institute, Beihang University, Hefei 230013, China*

Helin Li − *School of Integrated Circuit Science and Engineering, Beihang University, Beijing 100191, China*

Yongshan Liu − *School of Integrated Circuit Science and Engineering, Beihang University, Beijing 100191, China; Hefei Innovation Research Institute, Beihang University, Hefei 230013, China*

Fan Zhang − *School of Integrated Circuit Science and Engineering, Beihang University, Beijing 100191, China; Hefei Innovation Research Institute, Beihang University, Hefei 230013, China*

Houyi Cheng − *School of Integrated Circuit Science and Engineering, Beihang University, Beijing 100191, China; Hefei Innovation Research Institute, Beihang University, Hefei 230013, China*

Shina Tao − *College of Engineering and Applied Sciences, National Laboratory of Solid State Microstructures, Key Laboratory of Intelligent Optical Sensing and Manipulation, Collaborative Innovation Center of Advanced Microstructures, Nanjing University, Nanjing 210093, China*

Huacai Wang − *College of Engineering and Applied Sciences, National Laboratory of Solid State Microstructures, Key Laboratory of Intelligent Optical Sensing and Manipulation, Collaborative Innovation Center of Advanced Microstructures, Nanjing University, Nanjing 210093, China*

Wei Hu − *College of Engineering and Applied Sciences, National Laboratory of Solid State Microstructures, Key Laboratory of Intelligent Optical Sensing and Manipulation, Collaborative Innovation Center of Advanced Microstructures, Nanjing University, Nanjing 210093, China;* orcid.org/0000-0003-1255-9453

Yanqing Lu − *College of Engineering and Applied Sciences, National Laboratory of Solid State Microstructures, Key Laboratory of Intelligent Optical Sensing and Manipulation, Collaborative Innovation Center of Advanced Microstructures, Nanjing University, Nanjing 210093, China;* orcid.org/0000-0001-6151-8557

Chao Zhao − *School of Integrated Circuit Science and Engineering, Beihang University, Beijing 100191, China*

Complete contact information is available at: https://pubs.acs.org/10.1021/acsami.2c04782

Author Contributions

L.W., Q.G., and Y.S. conceived the idea. L.W., T.N., Q.G, W.H., C.Z., and W.Z. supervised the study. Y.S. performed the design, simulation, and measurements of the device. Y.X., F.Z., W.H., and Y.L. provided the experimental equipments. Y.L. and H.C. supported the thin film growth. H.L. and Y.S. prepared the metasurface. H.L., S.T., H.W., and Y.S. fabricated the integrated device. Y.S. analyzed the data and wrote the manuscript. All authors contributed to the discussion and preparation of the manuscript.

Notes

The authors declare no competing financial interest.

ACKNOWLEDGMENTS

We acknowledge financial support from the Key Project of Guangzhou and Shen Zhen joint foundation (2021B1515120012) and the National Key R&D Program of China (2018YFB0407602). Also, the STE in this work was supported by the National Natural Science Foundation of China (61774013 and 62105011) and Technology Major Project of Anhui Province (grant no. 202003a05020050). The devices were fabricated in Beihang-Goertek Joint Microelectronics Institute at Beihang University and National Laboratory of Solid State Microstructures at Nanjing University.

REFERENCES

(1) Stantchev, R. I.; Sun, B.; Hornett, S. M.; Hobson, P. A.; Gibson, G. M.; Padgett, M. J.; Hendry, E. Noninvasive, near-Field Terahertz Imaging of Hidden Objects Using a Single-Pixel Detector. *Sci. Adv.* **2016**, *2*, No. e1600190.

(2) Stantchev, R. I.; Yu, X.; Blu, T.; Pickwell-macpherson, E. Real-Time Terahertz Imaging with a Single-Pixel Detector. *Nat. Commun.* **2020**, *11*, 2535.

(3) Yang, Z.; Tang, D.; Hu, J.; Tang, M.; Zhang, M.; Cui, H. L.; Wang, L.; Chang, C.; Fan, C.; Li, J.; Wang, H. Near-Field Nanoscopic Terahertz Imaging of Single Proteins. *Small* **2020**, *17*, 2005814.

(4) Bai, Z.; Liu, Y.; Kong, R.; Nie, T.; Sun, Y.; Li, H.; Sun, T.; Pandey, C.; Wang, Y.; Zhang, H.; Song, Q.; Liu, G.; Kraft, M.; Zhao, W.; Wu, X.; Wen, L. Near-Field Terahertz Sensing of HeLa Cells and Pseudomonas Based on Monolithic Integrated Metamaterials with a Spintronic Terahertz Emitter. *ACS Appl. Mater. Interfaces* **2020**, *12*, 35895−35902.

(5) Wu, X.; Lu, H.; Sengupta, K. Programmable Terahertz Chip-Scale Sensing Interface with Direct Digital Reconfiguration at Sub-Wavelength Scales. *Nat. Commun.* **2019**, *10*, 2722.
(6) Karl, N. J.; Mckinney, R. W.; Monnai, Y.; Mendis, R.; Mittleman, D. M. Frequency-division multiplexing in the terahertz range using a leaky-wave antenna. *Nat. Photonics* **2015**, *9*, 717−720.
(7) Oshima, N.; Hashimoto, K.; Suzuki, S.; Asada, M. Terahertz Wireless Data Transmission With Frequency and Polarization Division Multiplexing Using Resonant-Tunneling-Diode Oscillators. *IEEE Trans. Terahertz Sci. Technol.* **2017**, *7*, 593−598.
(8) Koenig, S.; Lopez-Diaz, D.; Antes, J.; Boes, F.; Henneberger, R.; Leuther, A.; Tessmann, A.; Schmogrow, R.; Hillerkuss, D.; Palmer, R.; Zwick, T.; Koos, C.; Freude, W.; Ambacher, O.; Leuthold, J.; Kallfass, I. Wireless Sub-THz Communication System with High Data Rate. *Nat. Photonics* **2013**, *7*, 977−981.
(9) Yang, Y.; Yamagami, Y.; Yu, X.; Pitchappa, P.; Webber, J.; Zhang, B.; Fujita, M.; Nagatsuma, T.; Singh, R. Terahertz Topological Photonics for On-Chip Communication. *Nat. Photonics* **2020**, *14*, 446−451.
(10) Melinger, J. S.; Laman, N.; Grischkowsky, D. The Underlying Terahertz Vibrational Spectrum of Explosives Solids. *Appl. Phys. Lett.* **2008**, *93*, 011102.
(11) Pickwell, E.; Cole, B. E.; Fitzgerald, A. J.; Pepper, M.; Wallace, V. P. In vivo study of human skin using pulsed terahertz radiation. *Phys. Med. Biol.* **2004**, *49*, 1595−1607.
(12) Plusquellic, D. F.; Siegrist, K.; Heilweil, E. J.; Esenturk, O. Applications of Terahertz Spectroscopy in Biosystems. *ChemPhysChem* **2007**, *8*, 2412−2431.
(13) Choi, W. J.; Cheng, G.; Huang, Z.; Zhang, S.; Norris, T. B.; Kotov, N. A. Terahertz Circular Dichroism Spectroscopy of Biomaterials Enabled by Kirigami Polarization Modulators. *Nat. Mater.* **2019**, *18*, 820−826.
(14) Xu, W.; Xie, L.; Ying, Y. Mechanisms and Applications of Terahertz Metamaterial Sensing: A Review. *Nanoscale* **2017**, *9*, 13864−13878.
(15) Peng, Y.; Shi, C.; Zhu, Y.; Gu, M.; Zhuang, S. Terahertz Spectroscopy in Biomedical Field : A Review on Signal-to-Noise Ratio Improvement. *PhotoniX* **2020**, *1*, 12.
(16) Chen, H.-T.; Padilla, W. J.; Zide, J. M. O.; Gossard, A. C.; Taylor, A. J.; Averitt, R. D. Active Terahertz Metamaterial Devices. *Nature* **2006**, *444*, 597−600.
(17) Yu, N.; Capasso, F. Flat Optics with Designer Metasurfaces. *Nat. Mater.* **2014**, *13*, 139−150.
(18) He, J.; Dong, T.; Chi, B.; Zhang, Y. Metasurfaces for Terahertz Wavefront Modulation: a Review. *J. Infrared, Millimeter, Terahertz Waves* **2020**, *41*, 607−631.
(19) Guo, J.; Wang, T.; Zhao, H.; Wang, X.; Feng, S.; Han, P.; Sun, W.; Ye, J.; Situ, G.; Chen, H. T.; Zhang, Y. Reconfigurable Terahertz Metasurface Pure Phase Holograms. *Adv. Opt. Mater.* **2019**, *7*, 1801696.
(20) Venkatesh, S.; Lu, X.; Saeidi, H.; Sengupta, K. A High-Speed Programmable and Scalable Terahertz Holographic Metasurface Based on Tiled CMOS Chips. *Nat. Electron.* **2020**, *3*, 785−793.
(21) Shrestha, S.; Overvig, A. C.; Lu, M.; Stein, A.; Yu, N. Broadband Achromatic Dielectric Metalenses. *Light: Sci. Appl.* **2018**, *7*, 85.
(22) Chen, W. T.; Zhu, A. Y.; Sanjeev, V.; Khorasaninejad, M.; Shi, Z.; Lee, E.; Capasso, F. A Broadband Achromatic Metalens for Focusing and Imaging in the Visible. *Nat. Nanotechnol.* **2018**, *13*, 220−226.
(23) Lee, W. S. L.; Nirantar, S.; Headland, D.; Bhaskaran, M.; Sriram, S.; Fumeaux, C.; Withayachumnankul, W. Broadband Terahertz Circular-Polarization Beam Splitter. *Adv. Opt. Mater.* **2017**, *6*, 1700852.
(24) Zang, X.; Gong, H.; Li, Z. Metasurface for Multi-Channel Terahertz Beam Splitters and Polarization Rotators. *Appl. Phys. Lett.* **2018**, *112*, 171111.
(25) Cong, L.; Xu, N.; Han, J.; Zhang, W.; Singh, R. A Tunable Dispersion-Free Terahertz Metadevice with Pancharatnam-Berry-Phase-Enabled Modulation and Polarization Control. *Adv. Mater.* **2015**, *27*, 6630−6636.
(26) Yuan, Y.; Sun, S.; Chen, Y.; Zhang, K.; Ding, X.; Ratni, B.; Wu, Q.; Burokur, S. N.; Qiu, C. W. A Fully Phase-Modulated Metasurface as An Energy-Controllable Circular Polarization Router. *Adv. Sci.* **2020**, *7*, 2001437.
(27) Kindness, S. J.; Almond, N. W.; Michailow, W.; Wei, B.; Delfanazari, K.; Braeuninger-Weimer, P.; Hofmann, S.; Beere, H. E.; Ritchie, D. A.; Degl'Innocenti, R. A Terahertz Chiral Metamaterial Modulator. *Adv. Opt. Mater.* **2020**, *8*, 2000581.
(28) Han, Z.; Ohno, S.; Tokizane, Y.; Nawata, K.; Notake, T.; Takida, Y.; Minamide, H. Off-Resonance and in-Resonance Metamaterial Design for a High-Transmission Terahertz-Wave Quarter-Wave Plate. *Opt. Lett.* **2018**, *43*, 2977.
(29) Jia, M.; Wang, Z.; Li, H.; Wang, X.; Luo, W.; Sun, S.; Zhang, Y.; He, Q.; Zhou, L. Efficient Manipulations of Circularly Polarized Terahertz Waves with Transmissive Metasurfaces. *Light: Sci. Appl.* **2019**, *8*, 16.
(30) Xu, S.-T.; Fan, F.; Chen, S.; Xing, Y.; Gao, Y.; Li, H.; Niu, G.; Chang, S.-J. Electronically Controlled Liquid Crystal Terahertz Polarization Manipulation under Static Magnetic Field Pre-Anchoring. *Opt. Mater. Express* **2021**, *11*, 171.
(31) Sasaki, T.; Nishie, Y.; Kambayashi, M.; Sakamoto, M.; Noda, K.; Okamoto, H.; Kawatsuki, N.; Ono, H. Active Terahertz Polarization Converter Using a Liquid Crystal-Embedded Metal Mesh. *IEEE Photonics J.* **2019**, *11*, 1−7.
(32) Vasić, B.; Zografopoulos, D. C.; Isić, G.; Beccherelli, R.; Gajić, R. Electrically Tunable Terahertz Polarization Converter Based on Overcoupled Metal-Isolator-Metal Metamaterials Infiltrated with Liquid Crystals. *Nanotechnology* **2017**, *28*, 124002.
(33) Kindness, S. J.; Almond, N. W.; Michailow, W.; Wei, B.; Jakob, L. A.; Delfanazari, K.; Braeuninger-Weimer, P.; Hofmann, S.; Beere, H. E.; Ritchie, D. A.; Degl'Innocenti, R. Graphene-Integrated Metamaterial Device for All-Electrical Polarization Control of Terahertz Quantum Cascade Lasers. *ACS Photonics* **2019**, *6*, 1547−1555.
(34) Zhao, X.; Schalch, J.; Zhang, J.; Seren, H. R.; Duan, G.; Averitt, R. D.; Zhang, X. Electromechanically Tunable Metasurface Transmission Waveplate at Terahertz Frequencies. *Optica* **2018**, *5*, 303.
(35) Chen, X.; Wang, H.; Wang, C.; Ouyang, C.; Wei, G.; Nie, T.; Zhao, W.; Miao, J.; Li, Y.; Wang, L.; Wu, X. Efficient Generation and Arbitrary Manipulation of Chiral Terahertz Waves Emitted from Bi 2 Te 3 -Fe Heterostructures. *Adv. Photonics Res.* **2021**, *2*, 2000099.
(36) Kong, D.; Wu, X.; Wang, B.; Nie, T.; Xiao, M.; Pandey, C.; Gao, Y.; Wen, L.; Zhao, W.; Ruan, C.; Miao, J.; Li, Y.; Wang, L. Broadband Spintronic Terahertz Emitter with Magnetic-Field Manipulated Polarizations. *Adv. Opt. Mater.* **2019**, *7*, 1900487.
(37) Zhao, H.; Chen, X.; Ouyang, C.; Wang, H.; Kong, D.; Yang, P.; Zhang, B.; Wang, C.; Wei, G.; Nie, T.; Zhao, W.; Miao, J.; Li, Y.; Wang, L.; Wu, X. Generation and Manipulation of Chiral Terahertz Waves in the Three-Dimensional Topological. *Adv. Photonics* **2020**, *2*, 66003.
(38) Qiu, H.; Wang, L.; Shen, Z.; Kato, K.; Sarukura, N.; Yoshimura, M.; Hu, W.; Lu, Y.; Nakajima, M. Magnetically and Electrically Polarization-Tunable THz Emitter with Integrated Ferromagnetic Heterostructure and Large-Birefringence Liquid Crystal. *Appl. Phys. Express* **2018**, *11*, 092101.
(39) Liu, C.; Wang, S.; Zhang, S.; Cai, Q.; Wang, P.; Tian, C.; Zhou, L. Active Spintronic-Metasurface Terahertz Emitters with Tunable Chirality. *Adv. Photonics* **2021**, *3*, 056002.
(40) Kampfrath, T.; Battiato, M.; Maldonado, P.; Eilers, G.; Nötzold, J.; Mährlein, S.; Zbarsky, V.; Freimuth, F.; Mokrousov, Y.; Blügel, S.; Wolf, M.; Radu, I.; Oppeneer, P. M.; Münzenberg, M. Terahertz Spin Current Pulses Controlled by Magnetic Heterostructures. *Nat. Nanotechnol.* **2013**, *8*, 256−260.
(41) Bomzon, Z.; Biener, G.; Kleiner, V.; Hasman, E. Space-variant Pancharatnam-Berry phase optical elements with computer-generated subwavelength gratings. *Opt. Lett.* **2002**, *27*, 1141−1143.

https://doi.org/10.1021/acsami.2c04782
ACS Appl. Mater. Interfaces 2022, 14, 32646−32656

(42) Frisken, B. J. Nematic Liquid Crystals In Electric And Magnetic Fields. Ph.D Thesis, University of British Columbia, 1989.
(43) Seifert, T.; Jaiswal, S.; Martens, U.; Hannegan, J.; Braun, L.; Maldonado, P.; Freimuth, F.; Kronenberg, A.; Henrizi, J.; Radu, I.; Beaurepaire, E.; Mokrousov, Y.; Oppeneer, P. M.; Jourdan, M.; Jakob, G.; Turchinovich, D.; Hayden, L. M.; Wolf, M.; Münzenberg, M.; Kläui, M.; Kampfrath, T. Efficient Metallic Spintronic Emitters of Ultrabroadband Terahertz Radiation. *Nat. Photonics* **2016**, *10*, 483−488.
(44) Eimer, S.; Cheng, H.; Li, J.; Zhang, X.; Zhao, C. Perpendicular Magnetic Anisotropy Based Spintronics Devices in Pt/Co Stacks under Different Hard and Flexible Substrates. *Sci. China Inf. Sci.* **2021**, DOI: 10.1007/s11432-021-3371-4.
(45) Wang, L.; Lin, X.-w.; Liang, X.; Wu, J.-b.; Hu, W.; Zheng, Z.-g.; Jin, B.-b.; Qin, Y.-q.; Lu, Y.-q. Large Birefringence Liquid Crystal Material in Terahertz Range. *Opt. Mater. Express* **2012**, *2*, 1314.
(46) Wang, L.; Lin, X.-W.; Hu, W.; Shao, G.-H.; Chen, P.; Liang, L.-J.; Jin, B.-B.; Wu, P.-H.; Qian, H.; Lu, Y.-N.; Liang, X.; Zheng, Z.-G.; Lu, Y.-Q. Broadband Tunable Liquid Crystal Terahertz Waveplates Driven with Porous Graphene Electrodes. *Light: Sci. Appl.* **2015**, *4*, No. e253.
(47) Williams, R. Liquid Crystals in an Electric Field. *Nature* **1963**, *199*, 273−274.
(48) Durbin, S. D.; Arakelian, S. M.; Shen, Y. R. Optical-Field-Induced Birefringence and Freedericksz Transition in a Nematic Liquid Crystal. *Phys. Rev. Lett.* **1981**, *47*, 1411−1414.
(49) Chen, J. *Handbook of Visual Display Technology*; Springer, 2016.
(50) Huang, L.; Chen, X.; Mühlenbernd, H.; Li, G.; Bai, B.; Tan, Q.; Jin, G.; Zentgraf, T.; Zhang, S. Dispersionless Phase Discontinuities for Controlling Light Propagation. *Nano Lett.* **2012**, *12*, 5750−5755.
(51) Ding, X.; Monticone, F.; Zhang, K.; Zhang, L.; Gao, D.; Burokur, S. N.; De Lustrac, A.; Wu, Q.; Qiu, C.-W.; Alù, A. Ultrathin Pancharatnam-Berry Metasurface with Maximal Cross-Polarization Efficiency. *Adv. Mater.* **2015**, *27*, 1195−1200.
(52) Goldstein, D. H. *Polarized Light*, 3rd ed.; CRC Press, 2010.
(53) Xu, Y.; Li, Q.; Zhang, X.; Wei, M.; Xu, Q.; Wang, Q.; Zhang, H.; Zhang, W.; Hu, C.; Zhang, Z.; Zhang, C.; Zhang, X.; Han, J.; Zhang, W. Spin-Decoupled Multifunctional Metasurface for Asymmetric Polarization Generation. *ACS Photonics* **2019**, *6*, 2933−2941.
(54) Pendry, J. B.; Holden, A. J.; Robbins, D. J.; Stewart, W. J. Magnetism from Conductors and Enhanced Nonlinear Phenomena. *IEEE Trans. Microwave Theory Tech.* **1999**, *47*, 2075−2084.
(55) Walser, R. M.; Valanju, A. P.; Valanju, P. M. Comment on "Extremely Low Frequency Plasmons in Metallic Mesostructures". *Phys. Rev. Lett.* **2001**, *87*, 119701.
(56) Chen, H.-T.; O'Hara, J. F.; Taylor, A. J.; Averitt, R. D.; Highstrete, C.; Lee, M.; Padilla, W. J. Complementary Planar Terahertz Metamaterials. *Opt. Express* **2007**, *15*, 1084−1095.
(57) Arritt, B. J.; Smith, D. R.; Khraishi, T. Equivalent Circuit Analysis of Metamaterial Strain-Dependent Effective Medium Parameters. *J. Appl. Phys.* **2011**, *109*, 073512.
(58) Schurig, D.; Mock, J. J.; Smith, D. R. Electric-Field-Coupled Resonators for Negative Permittivity Metamaterials. *Appl. Phys. Lett.* **2006**, *88*, 041109.
(59) Loewenstein, E. V.; Smith, D. R.; Morgan, R. L. Optical Constants of Far Infrared Materials 2: Crystalline Solids. *Appl. Opt.* **1973**, *12*, 398.
(60) Grischkowsky, D.; Keiding, S.; van Exter, M.; Fattinger, C. Far-Infrared Time-Domain Spectroscopy with Terahertz Beams of Dielectrics and Semiconductors. *J. Opt. Soc. Am. B* **1990**, *7*, 2006.
(61) Lu, M.; Li, W.; Brown, E. R. Second-Order Bandpass Terahertz Filter Achieved by Multilayer Complementary Metamaterial Structures. *Opt. Lett.* **2011**, *36*, 1071.
(62) Liu, Y.; Cheng, H.; Xu, Y.; Vallobra, P.; Eimer, S.; Zhang, X.; Wu, X.; Nie, T.; Zhao, W. Separation of Emission Mechanisms in Spintronic Terahertz Emitters. *Phys. Rev. B* **2021**, *104*, 064419.
(63) Zhang, F.; Zhao, Q.; Kang, L.; Gaillot, D. P.; Zhao, X.; Zhou, J.; Lippens, D. Magnetic Control of Negative Permeability Metamaterials Based on Liquid Crystals. *Appl. Phys. Lett.* **2008**, *92*, 193104.
(64) Shen, Z.; Zhou, S.; Ge, S.; Duan, W.; Chen, P.; Wang, L.; Hu, W.; Lu, Y. Liquid-Crystal-Integrated Metadevice: Towards Active Multifunctional Terahertz Wave Manipulations. *Opt. Lett.* **2018**, *43*, 4695.
(65) Mcmaster, W. H. Polarization and the Stokes Parameters. *Am. J. Phys.* **1954**, *22*, 351.
(66) Milione, G.; Sztul, H. I.; Nolan, D. A.; Alfano, R. R. Higher-order Poincaré sphere, stokes parameters, and the angular momentum of light. *Phys. Rev. Lett.* **2011**, *107*, 053601.